New Concepts at the Interface: Novel Viewpoints and Interpretations, Theory and Computations

Polyelectrolyte-assisted oxygen vacancies: A new route to defect engineering in molybdenum oxide

Sajad Yazdani, Raana Kashfi-Sadabad, Huan Doan Tran, Mayra Daniela Morales-Acosta, and Michael Thompson Pettes

Langmuir, **Just Accepted Manuscript** • DOI: 10.1021/acs.langmuir.8b00539 • Publication Date (Web): 04 May 2018

Polyelectrolyte-assisted oxygen vacancies: A new route to defect engineering in molybdenum oxide

Sajad Yazdani,[a,†] Raana Kashfi-Sadabad,[b,†] Tran Doan Huan,[a,c] Mayra Daniela Morales-Acosta [b] and Michael Thompson Pettes[a,b,]*

[a] Department of Mechanical Engineering, University of Connecticut, Storrs, Connecticut 06269, USA.
[b] Institute of Materials Science, University of Connecticut, Storrs, Connecticut 06269, USA.
[c] Department of Materials Science and Engineering, University of Connecticut, Storrs, Connecticut 06269, USA.
[†] These authors contributed equally to this work.
[*] Author to whom correspondence should be addressed, email: michael.pettes@uconn.edu

Abstract. The presence of oxygen vacancy sites fundamentally affects physical and chemical properties of materials. In this study, a dipole-containing interaction between poly(diallyldimethylammonium chloride) PDDA and α-MoO_3 is found to enable high-concentrations of surface oxygen vacancies. Thermal annealing under Ar resulted in negligible reduction of MoO_3 to MoO_{3-x} with $x = 0.03$ at 600°C. In contrast, we show that thermochemical reaction with PDDA polyelectrolyte under Ar can significantly reduce MoO_3 to MoO_{3-x} with $x = 0.36$ ($MoO_{2.64}$) at 600°C. Thermal annealing under H_2 gas enhanced the sub-stoichiometry of MoO_{3-x} from $x = 0.62$ to 0.98 by using PDDA at the same conditions. Density functional theory calculations, supported by experimental analysis, suggest that the vacancy sites are created through absorption of terminal site oxygen (O_t) upon decomposition of the N─C bond in the pentagonal ring of PDDA during the thermal treatment. O_t atoms are absorbed as ionic O^- and neutral O^{2-}, creating Mo^{5+}-$v_O^{\cdot}$ and Mo^{4+}-$v_O^{\cdot\cdot}$ vacancy bipolarons and polarons, respectively. X-ray photoemission spectroscopy peak analysis indicates the ratio of charged to neutral molybdenum ions in the PDDA-processed samples increased from $Mo^{4+}/Mo^{6+} = 1.0$ and $Mo^{5+}/Mo^{6+} = 3.3$ when reduced at 400°C to $Mo^{4+}/Mo^{6+} = 3.7$ and $Mo^{5+}/Mo^{6+} = 2.6$ when reduced at 600°C. This is consistent with our *ab initio* calculation where the Mo^{4+}-$v_O^{\cdot\cdot}$ formation energy is 0.22 eV higher than that for Mo^{5+}-$v_O^{\cdot}$ in the bulk of the material and 0.02 eV higher on the surface. This study reveals a new paradigm for effective enhancement of surface oxygen vacancy concentrations

essential for a variety of technologies including advanced energy conversion applications such as low-temperature thermochemical water splitting.

Keywords: Molybdenum oxide, oxygen vacancy, PDDA polyelectrolyte, defect engineering, metal oxide, oxygen reduction

Introduction

The unique properties of Mo-based oxides including high electrochemical activity and mechanical and thermal durability make them ideal materials for development of many applications including efficient electrochemical energy storage systems.[1] Molybdenum oxidizes exist in a wide variety of structures and stoichiometries.[2] Among these, α-MoO_3 is layered with an orthorhombic structure[3] and monoclinic MoO_2 is known for high electrical conductivity.[4] Previous studies on these materials have been carried out in the fields of Li-ion batteries,[5] supercapacitors,[1, 3] hydrogen evolution reaction,[6] and oxygen reduction reaction.[7] The layered orthorhombic α-MoO_3 with multiple oxidation states is particularly attractive because of its potential for ion intercalation,[8] and its high work function (6.6 eV)[9] useful for organic light emitting diode (OLED)[10-13] applications.

MoO_3 is a highly redox-active material as multiple valence states (Mo^{6+}, Mo^{5+} and Mo^{4+}) have been reported to exist as a function of electrochemical potential,[8, 14-16] or by oxidation catalysis through interactions with methyl radicals.[17] Further reduction of Mo^{5+} to Mo^{4+} has been reported to occur through formation of a not fully-described intermediate specie by electrochemical electron transfer coupled with a chemical reaction.[8, 16] It has been reported that upon heating α-MoO_3 under vacuum for a long period of times (100 h at 700°C) a series of intermediate reduced M_nO_{3n-1} stoichiometries such as Mo_4O_{11},[18] $Mo_{17}O_{47}$, and Mo_8O_{23} are feasible with the most reduced form being MoO_2.[2] Formation of these reduced species involves a lattice rearrangement from corner-shared octahedra to an edge-shared octahedra with a shear structure.[2, 19] Spevack and McIntyre[19] reported that temperatures near 730°C were required in order to reduce MoO_3 thin films, originally synthesized at a low temperature (250°C), to MoO_2. Inzani and co-workers[20] investigated reduction of MoO_3 powders and solution-processed films under dilute (5%) hydrogen gas. Shear defects, nucleation and growth of reduced phases within the MoO_3 matrix were investigated. They reported that extended planar defects within the films acted as nucleation sites for Mo_4O_{11}.

Restructuring of the films upon reduction, in order to accommodate oxygen vacancies, was observed.

α-MoO_3 becomes an *n*-type semiconductor by presence of oxygen vacancies as an oxygen vacancy is a shallow donor in MoO_3 making MoO_{3-x} a degenerate *n*-type semiconductor.[9] Furthermore, the presence of oxygen vacancies have been shown to substantially alter physiochemical properties of MoO_3 such as optical properties[21, 22] and electrical conductivity.[23-25] Additionally, oxygen vacancy formation can increase interlayer distances,[21] which can potentially lead to improvement of electrochemical performance. Upon reduction of Mo^{6+} to Mo^{5+}, an additional conduction band above the valence band is formed through Mo^{5+}─Mo^{6+} interactions.[26] An additional charge carrier inserted into this conduction band causes a coupled lattice-electron distortion called polaron.[26, 27] A systematic shift of this polaron intervalence band in optical absorption spectra from 2.48 to 2.11 eV has been correlated to a decrease of the metal to oxygen ratio[26, 28]

The layered structure of α-MoO_3 consists of corner-sharing MoO_6 octahedra. This structure includes three oxygen atoms: symmetric (O_s), asymmetric (O_a), and terminal or bridging (O_t). O_a forms a long (2.25 Å) and a short (1.73 Å) asymmetric bond with two Mo atoms in the same sublayer and has 2-fold symmetry, whereas O_s contains 3-fold rotational symmetry with two equal bonds (1.95 Å) to Mo atoms in the same sublayer and a longer (2.33 Å) bond with a Mo atom in an adjacent sublayer. The shortest bond (1.67 Å) is Mo-O_t with only one Mo atom which is perpendicular to the stacking direction.[3, 29-32] Kim and Dunn *et al.*[3] investigated the effects of oxygen vacancies on the structure, chemistry, and charge storage properties of MoO_{3-x}. Using density functional theory (DFT) calculations, they found that a vacancy at oxygen terminal O_t site with two Mo^{5+} ions (bipolaron) near the defect center has the lowest formation enthalpy, and that formation of a Mo^{4+} polaron at the O_t site required slightly (0.19 eV) higher energy than bipolaron Mo^{5+}. Their calculations indicated that vacancy formation at asymmetric O_a and symmetric sites O_s were less favorable with energies of 1.17 eV (for O_a, Mo^{4+} polaron) and 2.09 eV (for O_s, Mo^{5+} bipolaron) higher than that of the O_t site with two Mo^{5+} ions (bipolaron). The reduced MoO_{3-x} retained the original structure during lithiation and delithiation, where incorporation of oxygen vacancies caused a larger interlayer spacing and led to faster charge transfer kinetics and higher specific capacity compared to the fully-oxidized MoO_3.[3] In addition, O_t vacancies have been

shown to be the catalytic active sites for various reactions including methane oxidation,[33] H_2O and CO adsorption,[34] hydrogen adsorption,[32, 35] methyl adsorption,[35] and reduction of NO.[36] Therefore, oxygen vacancies essentially determine physical properties as well as chemical activities of molybdenum oxides which is critical for many applications. This necessitates exploring and discovering effective approaches for the creation of high concentrations of oxygen vacancies in molybdenum oxides. In the present work, we report that the interaction between poly(diallyldimethylammonium chloride) (PDDA) and α-MoO_3 is capable of inducing these vacancies. Additionally, a new mechanism is proposed in order to explain the reduction reaction pathway between the charged polymer and the metal oxide surface using experiments and DFT calculations.

Experimental section

Chemicals. Pluronic P123 triblock poly(ethylene oxide)-*b*-poly(propylene oxide)-*b*-poly(ethylene oxide) copolymer (M_w = 5800, $EO_{20}PO_{70}EO_{20}$), 1-butanol (anhydrous, 99.8%), tetraethyl orthosilicate (TEOS), hydrochloric acid (HCl, 37%), ethyl alcohol (CH_3CH_2OH), phosphomolybdic acid (PMA, $H_3PMo_{12}O_{40}\cdot xH_2O$), poly(diallyldimethylammonium chloride) (PDDA) were purchased from Sigma-Aldrich Co. LLC. Hydrofluoric acid (HF, 49%) was purchased from Fischer Scientific Co. LLC. All chemicals were used as received.

Synthesis of mesoporous MoO_3. Based on a previously described procedure,[37] mesoporous silica SBA-15 was produced by hydrothermal synthesis a temperature of 100°C for 24 h. 4.4 g of PMA, as the Mo precursor, was impregnated into the channels of SBA-15 (1 g) already dispersed in 25 g of ethanol. The mixture was vigorously stirred for 3 h at room temperature. The nanocasting process was utilized through solvent evaporation[38, 39] of ethanol inside a petri dish placed at 60°C for 12 h. The obtained PMA/mesoporous silica nanocomposite (PMA@SBA-15) was calcined in air at 550°C with a rate of 1 °Cmin^{-1} for 4 h. The silica template in the obtained nanocomposite was removed through etching in a 4% HF aqueous solution.

Synthesis of MoO_{3-x}. 200 mg of mesoporous MoO_3 was dispersed in a solution of 200 mL of water:ethanol vol% 1:1. Then 100 µL of PDDA was added to the above solution. The mixture was intensely stirred for 24 hours at room temperature. The PDDA/MoO_3 product was obtained by

centrifugation and dried. The final samples were obtained by annealing at 400 and 600°C under Ar (100 sccm) and 5% H_2/95% Ar (20 sccm) for 3 hours with a ramp of 1 °Cmin^{-1}.

Characterization. A Bruker D2 Phaser with Cu Kα radiation (λ = 1.54184 Å) with an operating voltage and current of 30 kV and 10 mA at room temperature was used in order to perform powder X-ray diffraction (XRD) analysis. Quantitative determination of the phase composition was obtained through Rietveld refinement of the XRD patterns using MDI Jade software. The peak profile and background were fitted using a pseudo-Voigt and polynomial functions, respectively. Nitrogen adsorption-desorption isotherms were obtained at -196°C on a Quantachrome Instruments NOVA 2000e®. The degassing process was performed at 150°C under vacuum for a period of 6 h and the Brunauer–Emmett–Teller (BET) method was used in order to calculate the specific surface areas. The pore-size distributions of the samples were obtained by using the Barrett–Joyner–Halenda (BJH) method. Phase contrast transmission electron microscopy (TEM), selected area electron diffraction (SAED), and energy dispersive X-ray spectroscopy (EDS) were performed using a JEOL 2010 FasTEM at 200 kV. X-ray photoelectron spectroscopy (XPS) analysis was conducted on a PHI Model 590 spectrometer with multipoles (Φ Physical Electronics Industries Inc.), with Al Kα radiation (E_{photon} = 1486.6 eV). A TA Instruments Hi-Res TGA Q500 thermogravimetric analyzer was used to perform thermal gravimetric analysis (TGA) from 25 to 800°C at a heating rate of 10 °Cmin^{-1} and a flow rate of 60 mLmin^{-1} under air and nitrogen. TGA analysis on copper(II) oxalate hemihydrate (98%, Alfa Aesar No. A15365) under N_2 in order to make sure there was no leakage in the TGA furnace. This was confirmed by observing no oxidation in the TGA analysis as shown in Figure S1 in the supporting information. In addition, the error due to weight loss measurements was obtained by performing the TGA analysis of Pt under Air and N_2. The maximum error corresponding to the weight difference at 600°C was calculated as $x = \pm 0.005$. A TA Instruments SDT Q600 was used in order to perform differential scanning calorimetry (DSC) analysis on the samples from room temperature to 1200°C at a rate of 10 °Cmin^{-1} under Ar with a flow rate of 100 mLmin^{-1}. Zeta potential measurements were conducted on a Malvern Instruments Ltd Zetasizer Nano ZS.

Density functional theory calculations. The Vienna Ab initio Simulation Package (VASP),[40] was employed for conducting the density functional theory (DFT) calculations by adopting a basis set of plane waves with kinetic energies up to 500 eV. Exchange-correlation energies were

obtained by using Perdew-Burke-Ernzerhof functional[41] for all calculations. When the atomic forces calculated during the optimization fall below 0.01 eV/Å equilibrium structures were assumed. According to the method established by ref. 3, Dudarev's approach[42] was used to describe the *d* electrons of Mo. $U = 6.0$ eV was adopted for the onsite Coulomb term. The U value may be different across materials. For MoO_3, there are a number of values used by different researchers, who adopted different numerical details. These values include 5 eV,[43] 6.3 eV,[30, 44] 3eV and 7eV.[45] Here, U = 6 eV was chosen which, when combining with other details of the numerical scheme, produces reasonable geometry with respect to the experimental data. Using the optB88-vdW functional,[46, 47] the dispersion van der Waals interaction was calculated. Rozzi and co-workers[48] used a different approach with tight binding LMTO-ASA program with LDA.

For the polaron (Mo^{4+}) and bipolaron ($2 \times Mo^{5+}$) configurations, we adopted the procedure described in ref. 49, i.e. intentionally localizing/delocalizing the electron density at the interest Mo sites. Bulk MoO_3 models were constructed based on a 3×1×3 supercell of MoO_3. In order to model MoO_3 slabs, a vacuum layer in 10 Å thickness was appended to the bulk models, which uncovered O_t atoms on the (010) surface, and to suppress the interactions along the *y*-direction. This is the most stable surface of MoO_3 because of its layered structure. PDDA-MoO_3 interaction was assumed to be on this surface. The relaxed lattice parameters of $a = 3.930$ Å, $b = 13.951$ Å, and $c = 3.711$ Å were consistent with those reported in Ding *et al.*[46] Based on the performed Bader charge analysis, the charge for Mo^{6+}, Mo^{5+}, Mo^{4+}were obtained as 2.11e, 2.66e, and 3.12e, respectively. For these results, we note that we used 6 valence electrons for Mo.

Results and discussion

Mesoporous samples offer higher surface areas accessible for introduction of oxygen vacancies suitable for surface-chemistry related applications.[50] Thus, the nanocasting method using a SBA-15 silica hard template[37] was adopted in this work in order to effectively enhance the surface area of the samples. Figure 1 shows TEM analysis of the templated sample after calcination at 550°C in air and removal of silica SBA-15 template – subsequently denoted as fully oxidized O-MoO_3. A comparison between the TEM images of SBA-15 and O-MoO_3, indicate that the hexagonally-aligned nanowire structure of the parent template has been replicated, as shown in Figure 1a,b. The BET surface areas were obtained as 529 and 50 m^2g^{-1} for the SBA-15 silica hard template and

O-MoO_3, respectively. The BJH pore size distributions of the SBA-15 and O-MoO_3 were focused at 5.4 and 7.2 nm, respectively. The selected area electron diffraction (SAED) patterns and high resolution TEM of O-MoO_3 are shown in Figure 1c,d. SAED patterns were assigned to the orthorhombic phase of MoO_3 along the $[1\bar{1}2]$ zone axis, and the phase contrast image revealed that the sample was well crystallized. The EDS spectra of the mesoporous sample (Figure S2 in the supporting information) displays strong signals from elemental Mo and O with no signals from silicon, or other detectable impurities indicating the complete removal of the SBA-15 silica template after the HF etching process.

Figure 2 demonstrates the high angle XRD patterns for all samples. O-MoO_3 refers to the fully oxidized mesoporous sample templated by SBA-15, calcined at 550°C in air, and released by HF etching. By annealing the fully oxidized O-MoO_3 sample at 400 and 600°C under Ar or 5%H_2/95%Ar, MoO_{3-x}–400 and MoO_{3-x}–600 samples are obtained, respectively. The XRD patterns of the samples annealed under Ar (Figure 2a) were referenced to an orthorhombic α-MoO_3 with a space group Pbnm (space group 62) according to powder diffraction file #05-0508. From a comparison between the XRD patterns of MoO_{3-x}–400 and O-MoO_3, it can be found that annealing under Ar (400 and 600°C, 3 h) did not result in a full conversion of oxidized MoO_3 to other stoichiometries of the metal oxide. The weak peaks for MoO_{3-x}–600 are indexed to an orthorhombic phase of Mo_4O_{11} ($Pna2_1$, space group 33, powder diffraction file #84-0687) and to a triclinic phase of $Mo_{18}O_{52}$ (P-1, space group 2, powder diffraction file #74-1664), indicating weak reduction at 600°C – and negligible reduction at 400°C – occurs by thermal annealing. The Rietveld quantitative phase analysis indicates that the MoO_{3-x}–600 sample contains 55.8, 33.1 and 11.1 wt% of MoO_3, $Mo_{18}O_{52}$ and Mo_4O_{11}, respectively. In contrast, the XRD patterns of the oxidized O-MoO_3 sample indicate significant reductions of MoO_3 to MoO_{3-x} when thermally reacted with PDDA polyelectrolyte. These samples are denoted as MoO_{3-x}–PDDA-400 and MoO_{3-x}–PDDA-600 where Ar annealing was performed at 400 and 600°C, respectively. MoO_{3-x}–PDDA-400 pattern corresponds to the orthorhombic phase of MoO_3 (84 wt%) and the monoclinic phase of MoO_2 (16 wt%). MoO_{3-x}–PDDA-400 shows changes in the orientation of crystal planes along [020], [040] and [131] directions. Peak intensity ratios $I_{[040]}/I_{[110]} = 1.9$, $I_{[020]}/I_{[110]} = 1.3$, and $I_{[131]}/I_{[110]} = 0.9$ were measured for the MoO_3–PDDA-400 whereas values $I_{[040]}/I_{[110]} = 1.0$, $I_{[020]}/I_{[110]} = 1.0$ and $I_{[131]}/I_{[110]} = 0.4$ were obtained for the O-MoO_3 sample. However, by increasing

the annealing temperature to 600°C (sample MoO_{3-x}–PDDA-600), the XRD pattern indicates the presence of Mo_4O_{11} (61.4 wt%), MoO_2 (28.3 wt%) and $Mo_{18}O_{52}$ (2.21 wt%), as indicated in Figure 2. The results of XRD analysis demonstrate the strong oxygen reduction of the oxidized sample triggered by using a PDDA polyelectrolyte to enhance the thermal reduction reaction rate. Exhibiting more intense reduction compared to the samples annealed under Ar at the same conditions, the XRD patterns of the samples annealed under H_2-containing gas (5% H_2/95% Ar) indicated that both samples without and with PDDA were fully reduced to MoO_2 at 600°C for 3 h (Figure 2b).

The degree of reduction of the samples were calculated based on TGA analysis. The difference between the weight loss under air (assuming saturation to the fully oxidized O-MoO_3) and nitrogen (representing the reduced form, MoO_{3-x}) atmospheres were used to calculate the amount of vacancies, as illustrated in Figure 3. The sub-stoichiometry concentration x is calculated from the balance equation

$$M_w(MoO_3) = (1 + [(\%\ mass\ loss\ in\ air) - (\%\ mass\ loss\ in\ N_2)]/100) \times M_w(MoO_{3-x}) \qquad (1)$$

where M_w refers to the molecular weight. Table 1 contains the detailed information on thermal treatment conditions, Rietveld quantitative phase analysis and the sub-stoichiometry parameter x of the samples. For the oxidized samples reduced without the use of PDDA polymer, MoO_{3-x}–400 and MoO_{3-x}–600, the degrees of vacancies were calculated as $x = 0.01$, 0.03, respectively. This demonstrates negligible reduction of MoO_3 in the absence of PDDA. In contrast, degree of reduction of $x = 0.14$ ($MoO_{2.86}$) and 0.36 ($MoO_{2.64}$) were obtained for the reduction of oxidized samples with the use of PDDA after thermal annealing at 400°C (MoO_{3-x}–PDDA-400) and 600°C (MoO_{3-x}–PDDA-600), respectively. The weight loss due to PDDA decomposition is not observed as it was previously removed during the annealing process confirmed by TGA analysis of PDDA shown in Figure S3b. The TGA analyses indicated the PDDA interaction significantly enhanced the oxygen sub-stoichiometry concentrations under both Ar and 5% H_2/95% Ar atmospheres. Figure 2c and 2d compare the TGA analysis of the samples without and with PDDA, respectively, both pre-annealed under the H_2-containing gas. It was observed that using PDDA polyelectrolyte enhanced the weight difference between the oxidized and the reduces samples from 7.43 to 12.18% under 5% H_2/95% Ar at 600°C. Similar enhancement was seen from 3.06 to 8.2 at 400°C. As

calculated in Table 1, the sub-stoichiometry parameter x in MoO_{3-x} increased from 0.03 to 0.36 by using PDDA under Ar, and from 0.62 to 0.98 by using PDDA under 5% H_2/95% Ar gas. The results of TGA analysis are in agreement with our conclusions based on the XRD data. The reduction of samples with PDDA was further witnessed by differential scanning calorimetry (DSC) analysis showing a disappearance of the endothermic peak corresponding to the MoO_3 melting point at 798.6°C (Figure S3a, supporting information).

X-ray photoelectron spectroscopy (XPS) was employed in order to quantify the oxidation states in O-MoO_3, MoO_{3-x}–PDDA-400, and MoO_{3-x}–PDDA-600 samples (Figure 4). The survey XPS is shown in Figure S4 in the supporting information. The results indicated that MoO_3 involved only peaks assigned to Mo^{6+} in accordance to the XRD analysis. The high-resolution XPS analysis of MoO_{3-x}–PDDA-400 and MoO_{3-x}–PDDA-600 exhibited peaks assigned to both Mo^{4+} and Mo^{5+} which is a clear sign of reduction in these samples. The XPS surface area ratios of molybdenum oxidation states were calculated as $Mo^{4+}/Mo^{6+} = 1.0$ and $Mo^{5+}/Mo^{6+} = 3.3$ for the MoO_{3-x}–PDDA-400 sample reduced at 400°C, showing that its surface consisted primarily of $v_O^{\cdot}$ vacancy sites ($v_O^{\cdot}$ refers to an oxygen vacancy with a single positive charge according to Kröger-Vink notation). Area ratios of $Mo^{4+}/Mo^{6+} = 3.7$ and $Mo^{5+}/Mo^{6+} = 2.6$ were obtained for the MoO_{3-x}–PDDA-600 sample reduced at 600°C suggesting that $v_O^{\cdot\cdot}$ sites form the majority of the vacancy species when higher annealing temperatures are used ($v_O^{\cdot\cdot}$ refers to an oxygen vacancy with two positive charges according to Kröger-Vink notation). The area ratio of Mo^{4+} in MoO_{3-x}–PDDA-600 to Mo^{4+} in MoO_{3-x}–PDDA-400 was calculated as 2.7. Thus, as annealing temperature increases from 400 to 600°C, the ratio of Mo^{4+} increases significantly. This indicates that creation of Mo^{4+}-$v_O^{\cdot\cdot}$ vacancy complexes likely requires higher thermal energies. The fitting parameters for XPS Mo^{6+}, Mo^{5+}, and Mo^{4+} $3d_{3/2}$ and $3d_{5/2}$ spectral data and peak area ratios were compared with previous studies[51, 52] as presented in Table S1 in the supporting information.

In order to explain the strong reduction of MoO_3 by the PDDA polyelectrolyte, we propose the following mechanism obtained through theoretical modeling. The interface between the polymer and α-MoO_3 is illustrated in Figure 5a. PDDA is attracted to the surface of MoO_3 by strong electrostatic forces that originate from its electrolyte group. We have confirmed the electrostatic interaction experimentally by a zeta potential measurement where we observed a positive shift

from -53.3 mV for O-MoO_3 to -7.02 mV for MoO_{3-x}–PDDA-400 and -8.27 mV for MoO_{3-x}–PDDA-600. Based on the TGA analysis of PDDA shown in Figure S3b in the supporting information, the oxygen vacancy sites are created by absorption of O_t through decomposition of PDDA upon thermal annealing at temperatures above ~215°C. As a result, O_t atoms are absorbed as ionic O^- and neutral O^{2-}, causing the creation of Mo^{5+}-$v_O^{\cdot}$ and Mo^{4+}-$v_O^{\cdot\cdot}$ vacancy complexes, respectively. N─C and N─CH_3 bonds were investigated as the most possible bonds to break and absorb O_t. The energy associate with the absorption of O_t through breaking of these bonds are shown in Figure 5. The energy between the interface of PDDA and MoO_3 is defined as the reference. According to our calculations, O_t absorption through N─C bond in the pentagonal ring is the most plausible reaction for formation of both the $v_O^{\cdot\cdot}$ vacancy (3.37 eV) and the $v_O^{\cdot}$ vacancy (3.30 eV).

The formation energy of oxygen vacancy polarons in the bulk and surface MoO_{3-x} structures have been calculated and is shown in Figure 6. The DFT calculations were conducted based on the vacancy creations at O_t sites as this site advocates the lowest vacancy energy formation compared to asymmetric O_a and symmetric O_s oxygen.[3] O_t bonds with only one Mo site perpendicular to the layers in the structure, whereas O_a and O_s bond with two and three Mo atoms, respectively. Our DFT calculations suggest Mo^{4+} and Mo^{5+} as the most stable defect sites in both the surface and bulk of α-MoO_{3-x}. The formation energy of a Mo^{4+}-$v_O^{\cdot\cdot}$ vacancy complex was calculated as 0.22 and 0.02 eV higher than those of Mo^{5+}-$v_O^{\cdot\cdot}$ in the bulk and on the surface, respectively. Direct comparison between the Mo^{4+} and Mo^{5+} cases is allowed as we have used a bipolaron of Mo^{5+} to maintain an equal total number of electrons. The Mo^{5+} bipolaron configuration is taken as the lowest energy configuration from ref. 3. This indicates that the formation of Mo^{4+} vacancies is more favorable on the surface of the material compared to within the bulk. In addition, the slightly higher formation energy of Mo^{4+} compared to Mo^{5+} is in agreement with our XPS analysis which indicated the formation of Mo^{4+} required higher thermal energy. The creation of oxygen vacancies on the surface is essential for metal oxide catalytic activity where the surface is directly involved in the reaction.[53]

Furthermore, MoO_3 work function was calculated 6.83 eV above the Fermi energy, which was consistent with the results reported by Guo *et al.*[9] The calculated band gap of bulk MoO_3 was obtained as 1.70 eV, being consistent with 1.62 eV calculated by Huang *et al.*[47] Both of these

results are significantly lower than the true band gap of 3.3 eV (3.0–3.3 eV[9, 54]) because DFT with (semi) local XC functionals is well known to severely underestimate the solid band gap. To better estimate this important quantity, using the HSE06 hybrid XC functional[55] which is a standard way but at a tremendously higher computational cost. The band gaps of MoO_{3-x} were calculated using this scheme. Figure 7 demonstrates the calculated density of states (DOS), band gaps and the corresponding structures for MoO_{3-x} with $x = 0.0$, 0.17, and 0.33. The actual calculated band gap was 3.2201 eV for $x = 0.0$ and 2.8786 eV for $x = 0.17$. Interestingly, a metallic behavior with a band gap of 0.0 eV was calculated for $x = 0.33$.

In a previous study, Borgschulte *et al.*[56] reported the reduction of a 10 nm-thick MoO_3 thin film deposited on a Pd membrane using thermal evaporation by H_2 intercalation at room temperature. In order to investigate whether the H_2-containing gas treatment at room temperature induces considerable reduction in bulk scale powder MoO_3, 200 mg of Alfa Aesar No. 12930 (denoted as Ref. MoO_3) was kept under (5% H_2/95% Ar) at room temperature for 12 hours. The XRD patterns of the sample before the treatment and after the treatment are shown in Figure S5 in the supporting information. As can be observed, both patterns are assigned to MoO_3 orthorhombic phase indicating that no reduction in the bulk of the material has occurred due the room-temperature treatment. The calculation based on the TGA analysis of the treated sample shows a very small $x = 0.036$ even after heating to 600°C during the TGA analysis (Figure 8b). This negligible vacancy concentration seems to be from the vacancy initially present in the pristine Alfa Aesar No. 12930 sample by comparing the TGA results to that of the sample annealed under Ar with $x = 0.035$ as shown in Figure 8a. In addition, we investigated the effects of annealing time and PDDA concentration on the sub-stoichiometry of MoO_{3-x}. Based on the performed TGA analysis for Ref.-MoO_{3-x} samples, increasing the annealing time under Ar resulted in a large sub-stoichiometry parameter $x = 0.86$ (Figure 8c). In contrast, by increasing the PDDA concentration by 10 times from 100 to 1000 µl, $x = 0.42$ was obtained (Figure 8d). Thus, sub-stoichiometry appears to be more dependent on the annealing time compared to the polyelectrolyte concentration.

Conclusion

The thermochemical reaction mechanism between a PDDA polyelectrolyte and an α-MoO_3 metal oxide was determined by a combined experimental and theoretical investigation. Our

experiments indicated that if the fully oxidized MoO_3 is annealed at 400 and 600°C under Ar for 3 h, α-MoO_3 is negligibly reduced to MoO_{3-x} with $x = 0.01$, 0.03, respectively. In contrast, if the fully oxidized α-MoO_3 is treated with PDDA polyelectrolyte, significant vacancy concentrations form allowing transformation to MoO_{3-x}, where $x = 0.14$ ($MoO_{2.86}$) and 0.36 ($MoO_{2.64}$) were obtained for annealing temperatures of 400 and 600°C, respectively at the same conditions. Similar reduction behavior was observed under 5% H_2/95% Ar as the sub-stoichiometry x was increased from 0.62 to 0.98 by using the PDDA treatment. This phenomenon was explained by absorption of O_t upon decomposition of PDDA, where our DFT calculations suggested that O_t atoms were absorbed into the pentagonal ring of PDDA as ionic O^- and neutral O^{2-} creating Mo^{5+}-$v_O^{\cdot}$ and Mo^{4+}-$v_O^{\cdot\cdot}$ vacancy complexes on the metal oxide surface. Due to crucial role of oxygen vacancy concentration in determining physical or chemical properties of materials, the study of similar interactions of oxide materials with PDDA or other polymers in the polyelectrolyte family is suggested for future investigations.

Supporting Information

TGA analysis on copper(II) oxalate hemihydrate and Pt, EDS spectrum of O-MoO_3, DSC analysis of O- MoO_3, MoO_3–PDDA-400 and MoO_3–PDDA-600, TGA analysis of PDDA polymer, survey XPS spectra of O-MoO_3, MoO_3-PDDA-400 and MoO_3-PDDA-600 samples, fitting parameters for the XPS Mo^{6+}, Mo^{5+}, and Mo^{4+} $3d_{3/2}$ and $3d_{5/2}$ spectral data and peak area ratios, XRD patterns of bulk MoO_3.

Acknowledgements

Experimental work by R.K.-S., S.Y., and M.T.P. was partially supported by the National Science Foundation under Grant No. CBET-1553987 (M.T.P., S.Y., R.K.-S.), the UConn Research Foundation, award number PD17-0137 (M.T.P., R.K.-S., S.Y.), and a GE Graduate Fellowship for Innovation (S.Y.). Theoretical and computational work was conducted by T.D.H. and supported by XSEDE through the computational resource allocation number TG-DMR170031. TEM studies were conducted using facilities in the UConn/FEI Center for Advanced Microscopy and Materials Analysis (CAMMA). S.Y. and R.K.-S. contributed equally to this work.

References

(1) Hu, X.; Zhang, W.; Liu, X.; Mei, Y.; Huang, Y. Nanostructured Mo-based electrode materials for electrochemical energy storage, *Chem. Soc. Rev.* **2015**, *44*, 2376–2404. http://dx.doi.org/10.1039/C4CS00350K

(2) Greenwood, N. N.; Earnshaw, A. *Chemistry of the Elements*. 2nd ed.; Butterworth-Heinemann: New York, **1997**. ISBN: 978-0-7506-3365-9

(3) Kim, H.-S.; Cook, J. B.; Lin, H.; Ko, J. S.; Tolbert, S. H.; Ozolins, V.; Dunn, B. Oxygen vacancies enhance pseudocapacitive charge storage properties of MoO_{3-x}, *Nat. Mater.* **2017**, *16*, 454–460. http://dx.doi.org/10.1038/nmat4810

(4) Xie, Q.; Zheng, X.; Wu, D.; Chen, X.; Shi, J.; Han, X.; Zhang, X.; Peng, G.; Gao, Y.; Huang, H. High electrical conductivity of individual epitaxially grown MoO_2 nanorods, *Appl. Phys. Lett.* **2017**, *111*, 093505-1–5. http://dx.doi.org/10.1063/1.5001183

(5) Shi, Y.; Guo, B.; Corr, S. A.; Shi, Q.; Hu, Y.-S.; Heier, K. R.; Chen, L.; Seshadri, R.; Stucky, G. D. Ordered mesoporous metallic MoO_2 materials with highly reversible lithium storage capacity, *Nano Lett.* **2009**, *9*, 4215–4220. http://dx.doi.org/10.1021/nl902423a

(6) Chen, Z. P.; Ren, W. C.; Gao, L. B.; Liu, B. L.; Pei, S. F.; Cheng, H. M. Three-dimensional flexible and conductive interconnected graphene networks grown by chemical vapour deposition, *Nat. Mater.* **2011**, *10*, 424–428. http://dx.doi.org/10.1038/nmat3001

(7) Chandrasekaran, S.; Kim, E. J.; Chung, J. S.; Bowen, C. R.; Rajagopalan, B.; Adamaki, V.; Misra, R. D. K.; Hur, S. H. High performance bifunctional electrocatalytic activity of a reduced graphene oxide-molybdenum oxide hybrid catalyst, *J. Mater. Chem. A* **2016**, *4*, 13271–13279. http://dx.doi.org/10.1039/C6TA05043C

(8) Mendoza-Sánchez, B.; Brousse, T.; Ramirez-Castro, C.; Nicolosi, V.; Grant, P. S. An investigation of nanostructured thin film α-MoO_3 based supercapacitor electrodes in an aqueous electrolyte, *Electrochim. Acta* **2013**, *91*, 253–260. http://dx.doi.org/10.1016/j.electacta.2012.11.127

(9) Guo, Y.; Robertson, J. Origin of the high work function and high conductivity of MoO_3, *Appl. Phys. Lett.* **2014**, *105*, 222110-1–4. http://dx.doi.org/10.1063/1.4903538

(10) Meyer, J.; Khalandovsky, R.; Görrn, P.; Kahn, A. MoO_3 films spin-coated from a nanoparticle suspension for efficient hole-injection in organic electronics, *Adv. Mater.* **2011**, *23*, 70–73. http://dx.doi.org/10.1002/adma.201003065

(11) Greiner, M. T.; Helander, M. G.; Tang, W.-M.; Wang, Z.-B.; Qiu, J.; Lu, Z.-H. Universal energy-level alignment of molecules on metal oxides, *Nat. Mater.* **2011**, *11*, 76–81. http://dx.doi.org/10.1038/nmat3159

(12) Chen, Z.; Santoso, I.; Wang, R.; Xie, L. F.; Mao, H. Y.; Huang, H.; Wang, Y. Z.; Gao, X. Y.; Chen, Z. K.; Ma, D.; Wee, A. T. S.; Chen, W. Surface transfer hole doping of epitaxial graphene using MoO_3 thin film, *Appl. Phys. Lett.* **2010**, *96*, 213104-1–3. http://dx.doi.org/10.1063/1.3441263

(13) Meyer, J.; Kidambi, P. R.; Bayer, B. C.; Weijtens, C.; Kuhn, A.; Centeno, A.; Pesquera, A.; Zurutuza, A.; Robertson, J.; Hofmann, S. Metal oxide induced charge transfer doping and band alignment of graphene electrodes for efficient organic light emitting diodes, *Sci. Rep.* **2014**, *4*, 5380-1–7. http://dx.doi.org/10.1038/srep05380

(14) *Be, Ge, Mo, Si, Ti, W, Zn*. In Encyclopedia of Electrochemistry of the Elements, Bard, A. J., Ed. Marcel Dekker Inc. : New York, **1973**; Vol. 5. ISBN: 0824725050

(15) Anbananthan, N.; Nagaraja Rao, K.; Venkatesan, V. K. Cyclic voltammetric investigations of the reduction of Mo(VI) to Mo(IV) in 1 M sulphuric acid, *J. Electroanal. Chem.* **1994**, *374*, 207–214. http://dx.doi.org/10.1016/0022-0728(94)03356-0

(16) Anbananthan, N.; Nagaraja Rao, K.; Venkatesan, V. K. Electrochemical formation of oxygen-deficient molybdenum oxide, *Appl. Surf. Sci.* **1993**, *72*, 189–194. http://dx.doi.org/10.1016/0169-4332(93)90011-Y

(17) Tong, Y.; Lunsford, J. H. Mechanistic and kinetic studies of the reactions of gas-phase methyl radicals with metal oxides, *J. Am. Chem. Soc.* **1991**, *113*, 4741–4746. http://dx.doi.org/10.1021/ja00013a005

(18) Magnéli, A. The crystal structure of Mo_4O_{11} (γ-molybdenum oxide), *Acta Chem. Scand.* **1948**, *2*, 861–871. http://dx.doi.org/10.3891/acta.chem.scand.02-0861

(19) Spevack, P. A.; McIntyre, N. S. Thermal reduction of molybdenum trioxide, *J. Phys. Chem.* **1992**, *96*, 9029–9035. http://dx.doi.org/10.1021/j100201a062

(20) Inzani, K.; Nematollahi, M.; Selbach, S. M.; Grande, T.; Vullum-Bruer, F. Progression of reduction of MoO_3 observed in powders and solution-processed films, *Thin Solid Films* **2017**, *626*, 94–103. http://dx.doi.org/10.1016/j.tsf.2017.02.029

(21) Dieterle, M.; Weinberg, G.; Mestl, G. Raman spectroscopy of molybdenum oxides Part I. Structural characterization of oxygen defects in MoO_{3-x} by DR UV/VIS, Raman spectroscopy and X-ray diffraction, *Phys. Chem. Chem. Phys.* **2002**, *4*, 812–821. http://dx.doi.org/10.1039/B107012F

(22) Dzhanelidze, R. B.; Purtseladze, I. M.; Khitarishvili, L. S.; Chikovani, R. I.; Shkol'nik, A. L. Some optical and photoelectric properties of molybdenum oxide, *Sov. Phys. Solid State* **1966**, *7*, 2082–2083.

(23) Hu, X. K.; Qian, Y. T.; Song, Z. T.; Huang, J. R.; Cao, R.; Xiao, J. Q. Comparative study on MoO_3 and H_xMoO_3 nanobelts: Structure and electric transport, *Chem. Mater.* **2008**, *20*, 1527–1533. http://dx.doi.org/10.1021/cm702942y

(24) Balendhran, S.; Deng, J.; Ou, J. Z.; Walia, S.; Scott, J.; Tang, J.; Wang, K. L.; Field, M. R.; Russo, S.; Zhuiykov, S.; Strano, M. S.; Medhekar, N.; Sriram, S.; Bhaskaran, M.; Kalantar-Zadeh, K. Enhanced charge carrier mobility in two-dimensional high dielectric molybdenum oxide, *Adv. Mater.* **2013**, *25*, 109–114. http://dx.doi.org/10.1002/adma.201203346

(25) Gruber, H.; Krautz, E. Untersuchungen der elektrischen leitfähigkeit und des magnetowiderstandes im system molybdän-sauerstoff, *Phys. Status Solidi A* **1980**, *62*, 615–624. http://dx.doi.org/10.1002/pssa.2210620233

(26) Mestl, G.; Verbruggen, N. F. D.; Knoezinger, H. Mechanically activated MoO_3. 2. Characterization of defect structures, *Langmuir* **1995**, *11*, 3035–3041. http://dx.doi.org/10.1021/la00008a031

(27) Tilley, R. J. D. *Defect Crystal Chemistry and its Applications*. Blackie & Son: London, **1987**. ISBN: 0412013312

(28) Porter, V. R.; White, W. B.; Roy, R. Optical spectra of the intermediate oxides of titanium, vanadium, molybdenum, and tungsten, *J. Solid State Chem.* **1972**, *4*, 250–254. http://dx.doi.org/10.1016/0022-4596(72)90113-2

(29) Kihlborg, L. The structural chemistry of the higher molybdenum oxides, *Ark. Kemi.* **1963**, *21*, 357–364.

(30) Coquet, R.; Willock, D. J. The (010) surface of α-MoO_3, a DFT+U study, *Phys. Chem. Chem. Phys.* **2005**, *7*, 3819–3828. http://dx.doi.org/10.1039/B511044K

(31) Cora, F.; Patel, A.; Harrison, N. M.; Roetti, C.; Richard A. Catlow, C. An *ab initio* Hartree-Fock study of α-MoO_3, *J. Mater. Chem.* **1997**, *7*, 959–967. http://dx.doi.org/10.1039/A607439A

(32) Chen, M.; Waghmare, U. V.; Friend, C. M.; Kaxiras, E. A density functional study of clean and hydrogen-covered α-MoO_3(010): Electronic structure and surface relaxation, *J. Chem. Phys.* **1998**, *109*, 6854–6860. http://dx.doi.org/10.1063/1.477252

(33) Smith, M. R.; Ozkan, U. S. The partial oxidation of methane to formaldehyde: Role of different crystal planes of MoO_3, *J. Catal.* **1993**, *141*, 124–139. http://dx.doi.org/10.1006/jcat.1993.1124

(34) Papakondylis, A.; Sautet, P. *Ab initio* study of the structure of the α-MoO_3 solid and study of the adsorption of H_2O and CO molecules on its (100) surface, *J. Phys. Chem.* **1996**, *100*, 10681–10688. http://dx.doi.org/10.1021/jp953727w

(35) Chen, M.; Friend, C. M.; Kaxiras, E. The chemical nature of surface point defects on MoO_3(010): Adsorption of hydrogen and methyl, *J. Am. Chem. Soc.* **2001**, *123*, 2224–2230. http://dx.doi.org/10.1021/ja994376s

(36) Remediakis, I. N.; Kaxiras, E.; Chen, M.; Friend, C. M. Dinitrosyl formation as an intermediate stage of the reduction of NO in the presence of MoO_3, *J. Chem. Phys.* **2003**, *118*, 6046–6051. http://dx.doi.org/10.1063/1.1556846

(37) Zhao, D.; Feng, J.; Huo, Q.; Melosh, N.; Fredrickson, G. H.; Chmelka, B. F.; Stucky, G. D. Triblock copolymer syntheses of mesoporous silica with periodic 50 to 300 angstrom pores, *Science* **1998**, *279*, 548–552. http://dx.doi.org/10.1126/science.279.5350.548

(38) Shi, Y.; Wan, Y.; Zhang, R.; Zhao, D. Synthesis of self-supported ordered mesoporous cobalt and chromium nitrides, *Adv. Funct. Mater.* **2008**, *18*, 2436–2443. http://dx.doi.org/10.1002/adfm.200800488

(39) Dickinson, C.; Zhou, W.; Hodgkins, R. P.; Shi, Y.; Zhao, D.; He, H. Formation mechanism of porous single-crystal Cr_2O_3 and Co_3O_4 templated by mesoporous silica, *Chem. Mater.* **2006**, *18*, 3088–3095. http://dx.doi.org/10.1021/cm060014p

(40) Kresse, G.; Furthmüller, J. Efficient iterative schemes for *ab initio* total-energy calculations using a plane-wave basis set, *Phys. Rev. B* **1996**, *54*, 11169–11186. http://dx.doi.org/10.1103/PhysRevB.54.11169

(41) Perdew, J. P.; Burke, K.; Ernzerhof, M. Generalized gradient approximation made simple, *Phys. Rev. Lett.* **1996**, *77*, 3865–3868. http://dx.doi.org/10.1103/PhysRevLett.77.3865

(42) Dudarev, S. L.; Botton, G. A.; Savrasov, S. Y.; Humphreys, C. J.; Sutton, A. P. Electron-energy-loss spectra and the structural stability of nickel oxide: An LSDA+U study, *Phys. Rev. B* **1998**, *57*, 1505–1509. http://dx.doi.org/10.1103/PhysRevB.57.1505

(43) Inzani, K.; Grande, T.; Vullum-Bruer, F.; Selbach, S. M. A van der Waals density functional study of MoO_3 and its oxygen vacancies, *J. Phys. Chem. C* **2016**, *120*, 8959–8968. http://dx.doi.org/10.1021/acs.jpcc.6b00585

(44) Lei, Y.-H.; Chen, Z.-X. DFT+U study of properties of MoO_3 and hydrogen adsorption on MoO_3(010), *J. Phys. Chem. C* **2012**, *116*, 25757–25764. http://dx.doi.org/10.1021/jp304122n

(45) Baldoni, M.; Craco, L.; Seifert, G.; Leoni, S. A two-electron mechanism of lithium insertion into layered α-MoO_3: A DFT and DFT+U study, *J. Mater. Chem. A* **2013**, *1*, 1778–1784. http://dx.doi.org/10.1039/C2TA00839D

(46) Ding, H.; Ray, K. G.; Ozolins, V.; Asta, M. Structural and vibrational properties of α-MoO_3 from van der Waals corrected density functional theory calculations, *Phys. Rev. B* **2012**, *85*, 012104-1–4. http://dx.doi.org/10.1103/PhysRevB.85.012104

(47) Huang, P.-R.; He, Y.; Cao, C.; Lu, Z.-H. Impact of lattice distortion and electron doping on α-MoO_3 electronic structure, *Sci. Rep.* **2014**, *4*, 7131-1–7. http://dx.doi.org/10.1038/srep07131

(48) Rozzi, C. A.; Manghi, F.; Parmigiani, F. *Ab initio* Fermi surface and conduction-band calculations in oxygen-reduced MoO_3, *Phys. Rev. B* **2003**, *68*, 075106-1–6. http://dx.doi.org/10.1103/PhysRevB.68.075106

(49) Deskins, N. A.; Dupuis, M. Electron transport via polaron hopping in bulk TiO_2: A density functional theory characterization, *Phys. Rev. B* **2007**, *75*, 195212-1–10. http://dx.doi.org/10.1103/PhysRevB.75.195212

(50) Li, W.; Liu, J.; Zhao, D. Mesoporous materials for energy conversion and storage devices, *Nat. Rev. Mater.* **2016**, *1*, 16023-1–17. http://dx.doi.org/10.1038/natrevmats.2016.23

(51) Inzani, K.; Nematollahi, M.; Vullum-Bruer, F.; Grande, T.; Reenaas, T. W.; Selbach, S. M. Electronic properties of reduced molybdenum oxides, *Phys. Chem. Chem. Phys.* **2017**, *19*, 9232–9245. http://dx.doi.org/10.1039/C7CP00644F

(52) Scanlon, D. O.; Watson, G. W.; Payne, D. J.; Atkinson, G. R.; Egdell, R. G.; Law, D. S. L. Theoretical and experimental study of the electronic structures of MoO_3 and MoO_2, *J. Phys. Chem. C* **2010**, *114*, 4636–4645. http://dx.doi.org/10.1021/jp9093172

(53) Ruiz Puigdollers, A.; Schlexer, P.; Tosoni, S.; Pacchioni, G. Increasing oxide reducibility: The role of metal/oxide interfaces in the formation of oxygen vacancies, *ACS Catal.* **2017**, *7*, 6493–6513. http://dx.doi.org/10.1021/acscatal.7b01913

(54) Kröger, M.; Hamwi, S.; Meyer, J.; Riedl, T.; Kowalsky, W.; Kahn, A. Role of the deep-lying electronic states of MoO_3 in the enhancement of hole-injection in organic thin films, *Appl. Phys. Lett.* **2009**, *95*, 123301-1–3. http://dx.doi.org/10.1063/1.3231928

(55) Heyd, J.; Scuseria, G. E.; Ernzerhof, M. Erratum: “Hybrid functionals based on a screened Coulomb potential” [J. Chem. Phys. 118, 8207 (2003)], *J. Chem. Phys.* **2006**, *124*, 219906-1. http://dx.doi.org/10.1063/1.2204597

(56) Borgschulte, A.; Sambalova, O.; Delmelle, R.; Jenatsch, S.; Hany, R.; Nüesch, F. Hydrogen reduction of molybdenum oxide at room temperature, *Sci. Rep.* **2017**, *7*, 40761-1–9. http://dx.doi.org/10.1038/srep40761

Figures and Figure Captions

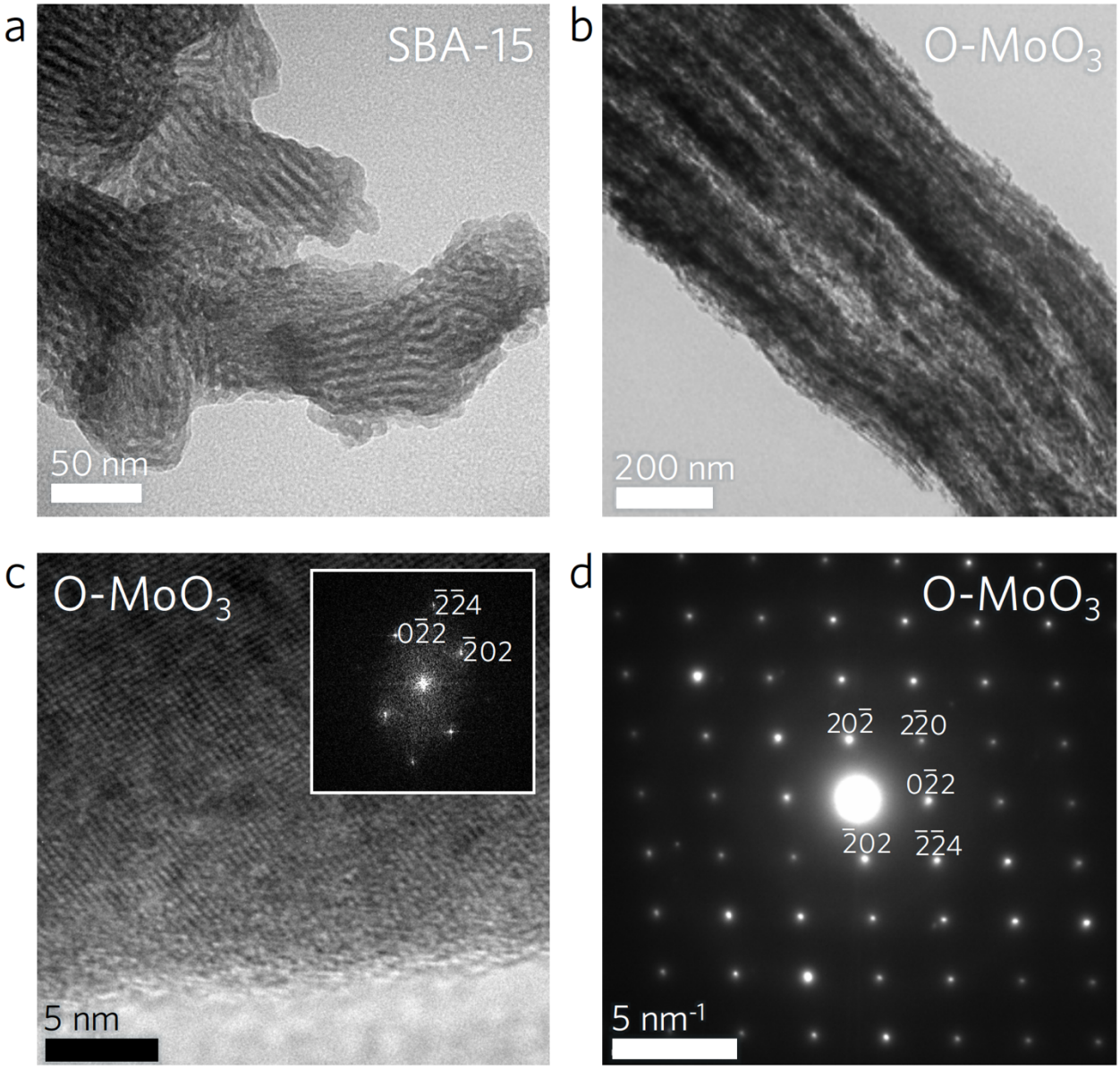

Figure 1. Transmission electron microscopy (TEM) analysis of SBA-15 silica hard template and mesoporous fully oxidized O-MoO_3. TEM images of mesoporous (a) SBA-15 and (b) O-MoO_3. (c) High resolution TEM of O-MoO_3 and (c, inset) fast Fourier transform (FFT). (d) selected area electron diffraction (SAED) pattern along the [$1\bar{1}2$] zone axis for O-MoO_3.

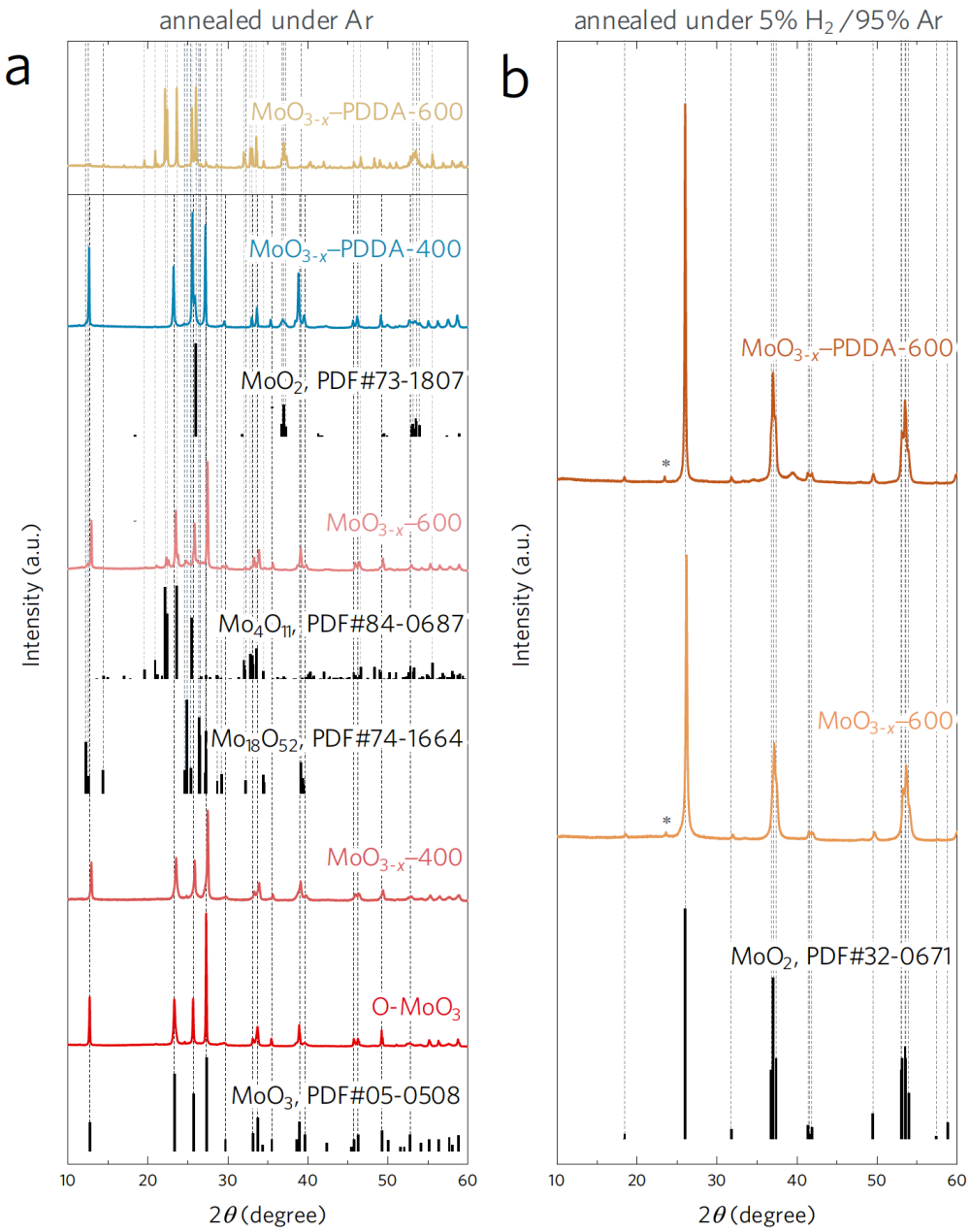

Figure 2. X-ray diffraction (XRD) analysis reveals routes to creating sub-stoichiometric MoO_3. XRD patterns for the mesoporous fully oxidized O-MoO_3, oxidized samples annealed under Ar without PDDA polymer (MoO_{3-x}–400 and MoO_{3-x}–600) at 400 and 600°C under Ar respectively, and oxidized samples annealed under Ar with PDDA polymer (MoO_{3-x}–PDDA-400 and MoO_{3-x}–PDDA-600) at 400 and 600°C under Ar respectively. (b) XRD patterns of MoO_{3-x}–600 (sample with no PDDA) and MoO_{3-x}–PDDA-600 (sample with PDDA) annealed under 5% H_2/95% Ar at 600°C. The weak peak at $2\theta = 23.4°$ (asterisks) is due to K-beta emission from the copper anode of the X-ray diffractometer.

Table 1. Detailed annealing conditions, Rietveld refinement phase analysis and oxygen sub-stoichiometry concentration "*x*" in MoO_{3-x} determined by thermogravimetric analysis as given by equation (1).

Sample ID	Annealing conditions			Annealing gas	Rietveld refinement				*x* (±0.005) based on TGA
	Temperature (°C)	Rate (°C min^{-1})	Time (h)		MoO_3	$Mo_{18}O_{52}$	$Mo_{18}O_{52}$	MoO_2	
O-MoO_3	550	1	4	Air	100%	--	--	--	0.00
MoO_{3-x}–400	400	1	3	Ar	100%	--	--	--	--
MoO_{3-x}–600	600	1	3	Ar	55.8%	33.1%	11.1%	--	0.03
MoO_{3-x}–PDDA-400	400	1	3	Ar	84.0%	--	--	16.0%	--
MoO_{3-x}–PDDA-600	600	1	3	Ar	--	61.4%	10.3%	28.3%	0.36
MoO_{3-x}–600	600	1	3	5%H_2/95%Ar	--	--	--	100%	0.62
MoO_{3-x}–PDDA-600	600	1	3	5%H_2/95%Ar	--	--	--	100%	0.98

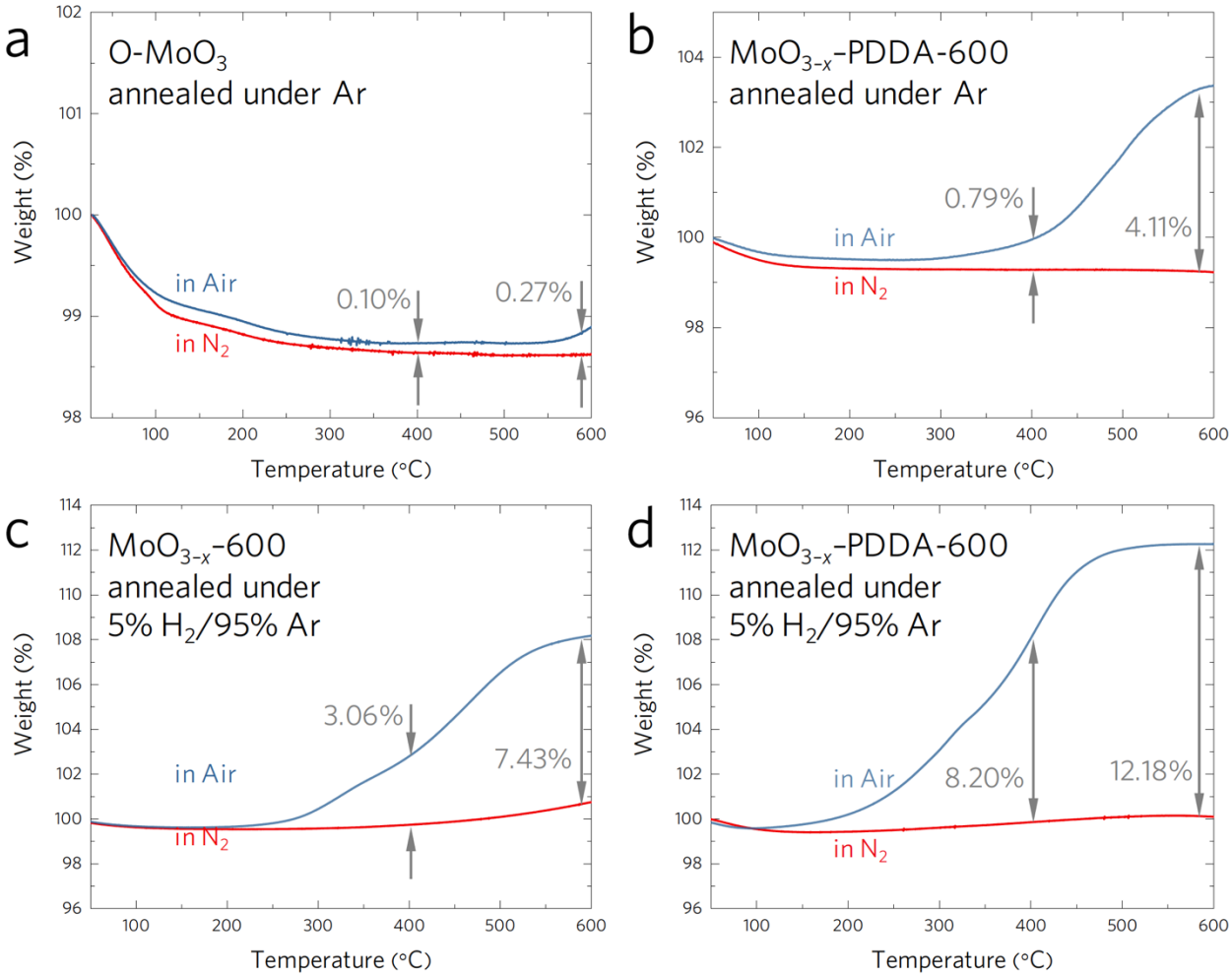

Figure 3. Thermogravimetric analysis (TGA) indicates PDDA treatment is effective reduction of MoO_3. Air and nitrogen TGA analysis of: (a) O-MoO_3 (sample without PDDA), (b) MoO_{3-x}–PDDA-600 (sample with PDDA) annealed under Ar at 600°C, (c) MoO_{3-x}–600 (sample without PDDA) annealed under 5%H2/95%Ar at 600°C, and (d) MoO_{3-x}–PDDA-600 (sample with PDDA) annealed under 5% H_2/95% Ar at 600°C. Using the comparison between the weight loss/gain in air and nitrogen, the value of x is quantified according to equation (1). Prior to TGA characterization, both samples were annealed under the specified gas at 600°C for 3 hours. For this reason, weight loss due to PDDA decomposition did not appear in the obtained data as the polyelectrolyte was removed during the annealing process. Therefore, any weight loss/gain can be ascribed to oxygen sub-stoichiometry.

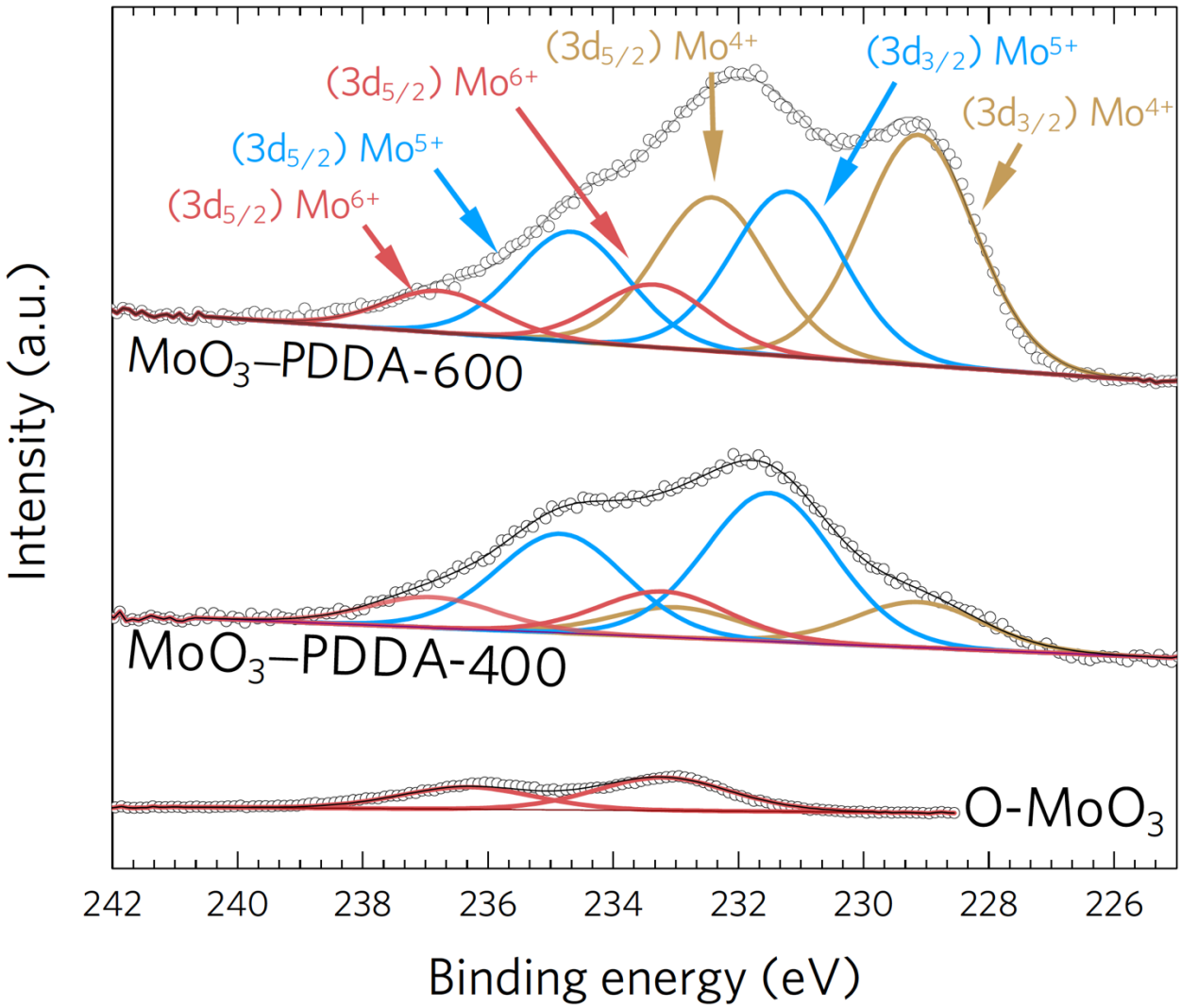

Figure 4. X-ray photoelectron spectroscopy (XPS) indicates valence state of oxygen vacancy defects created by metal oxide/PDDA interaction. Deconvolved Mo 3d XPS spectra of pure mesoporous fully oxidized O-MoO_3 and of reduced MoO_{3-x}–PDDA-400 and MoO_{3-x}–PDDA-600 samples.

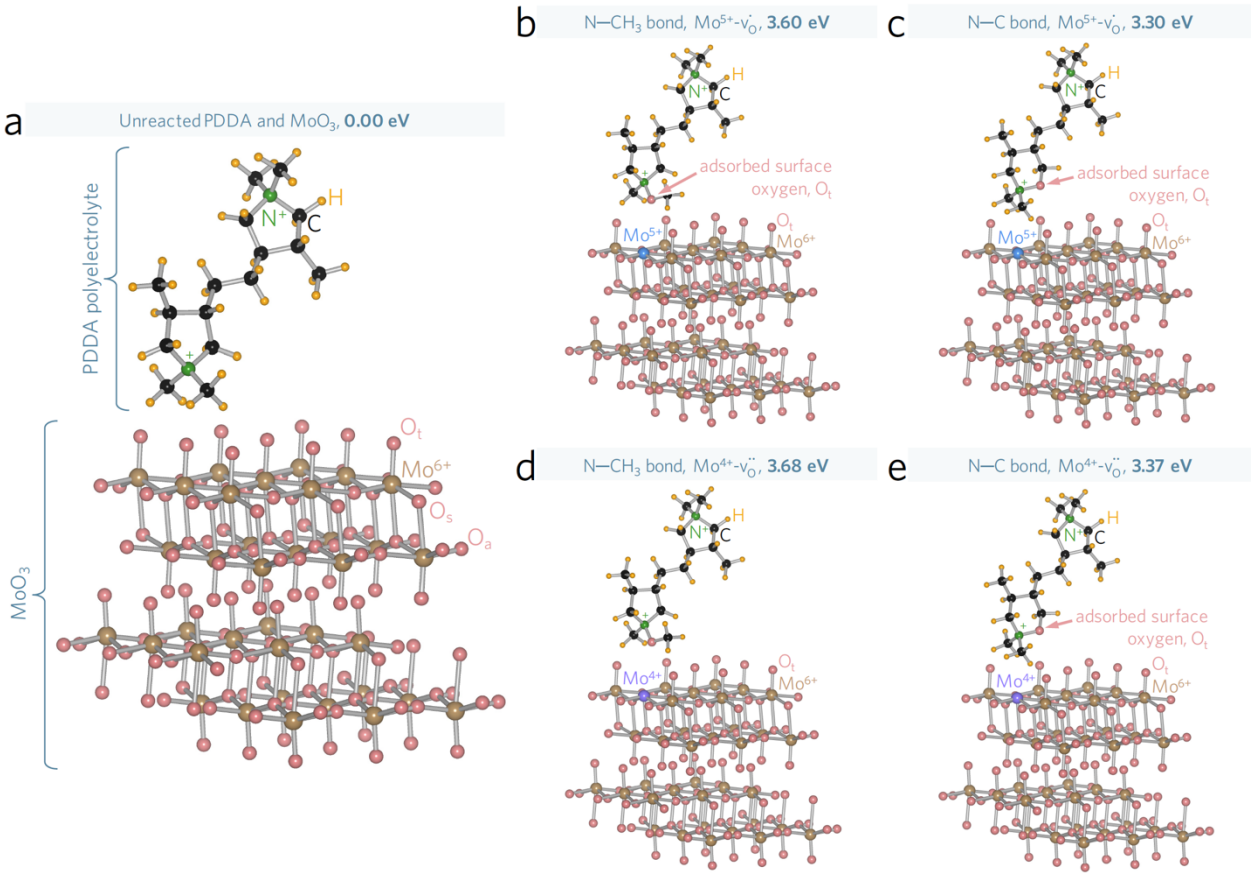

Figure 5. Density functional theory (DFT) calculations elucidate a pathway for PDDA-assisted reduction of α-MoO_3 to α-MoO_{3-x}. (a) Interface between the PDDA polyelectrolyte (positively charged molecule) and the surface of α-MoO_3 is used as the reference state for DFT calculations, where two monomers are modeled as the repeating unit of PDDA to minimize the dipole-dipole interaction. (b-e) DFT calculations of the energy required for bond-breaking and insertion of a surface oxygen atom, O_t, by a PDDA polyelectrolyte molecule in order to create (b, c) Mo^{5+}-$v_O^{\cdot}$ and (d, e) Mo^{4+}-$v_O^{\cdot\cdot}$ vacancy complexes through the breaking of (b, d) a N─CH_3 bond and (c, e) a N─C bond in the pentagonal ring of PDDA.

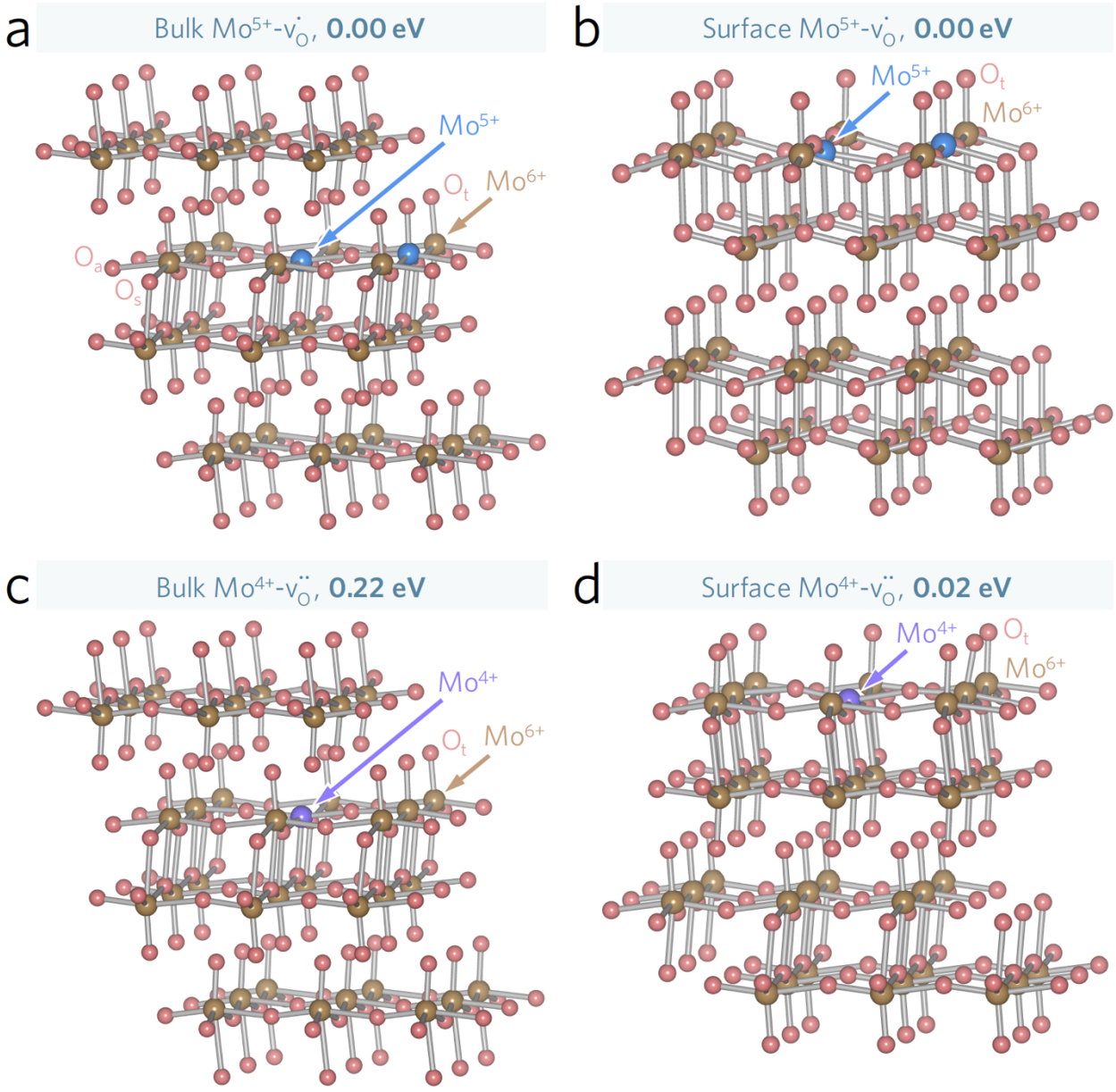

Figure 6. DFT calculations of the internal energy of formation for oxygen vacancies in α-MoO_{3-x}. (a) Bulk and (b) surface bipolaron of Mo^{5+} and (c) bulk and (d) surface polaron of Mo^{4+}. The bipolaron configuration in (a,b) is based on the lowest energy configuration given in ref. 3. The internal energy in (c,d) is referenced to that of (a,b) respectively to highlight the difference between Mo^{4+} and Mo^{5+} oxidation state formation, where a bipolaron of Mo^{5+} is used to enable direct comparison as the total number of electrons is equal in all panels.

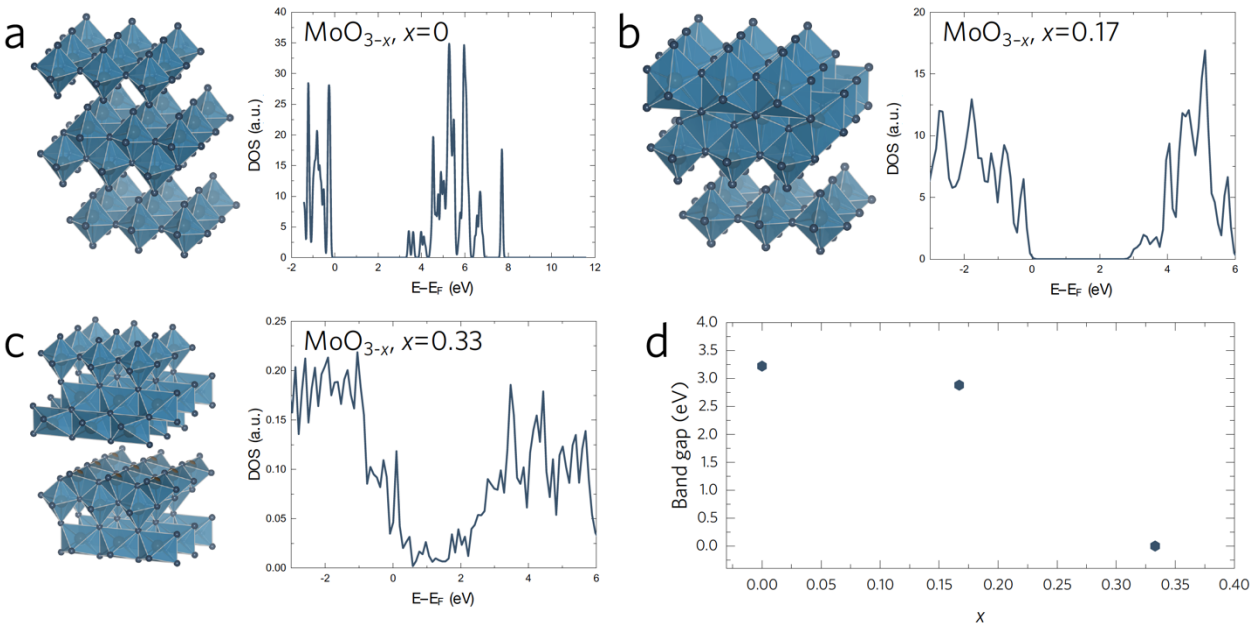

Figure 7. ***Ab initio*** **electronic density of states and band gap of MoO_{3-x}.** Calculated DOS using the optB88-vdW exchange correlation functional for (a) $x = 0.0$, (b) $x = 0.17$, and (c) $x = 0.33$. (d) Electronic band gaps for different oxygen vacancy concentrations calculated using the HSE06 hybrid XC functional.

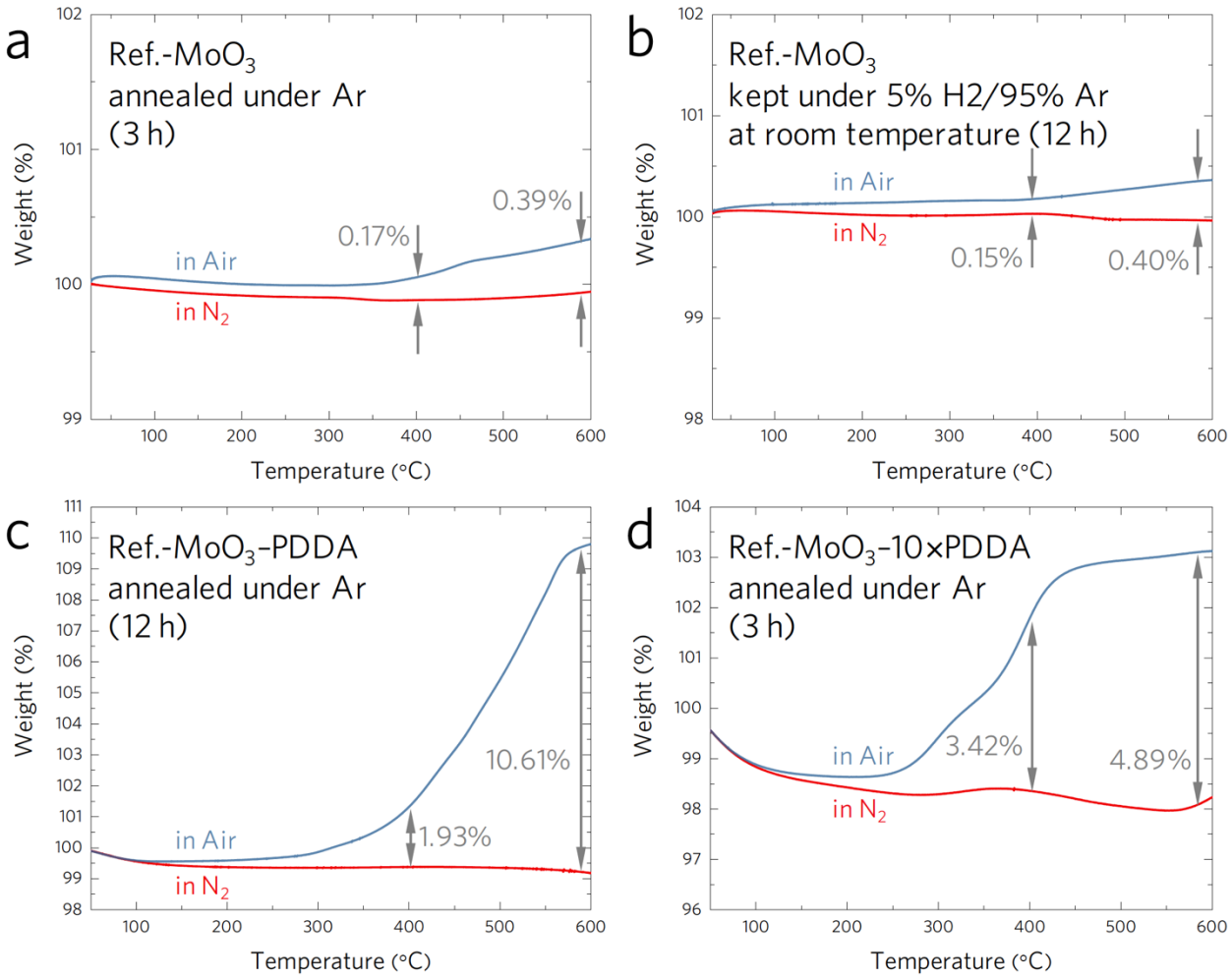

Figure 8. Thermogravimetric analysis (TGA) indicating the effects of annealing temperature, time, and PDDA concentration on reduction of MoO_3. Air and nitrogen TGA analysis of: (a) Ref.-MoO_3 (Alfa Aesar No. 12930, without PDDA) annealed under Ar at 600°C for 3 h, (b) Ref.-MoO_3 kept under 5% H_2 in Ar at room temperature for 12 h, (c) Ref.-MoO_3–PDDA (Alfa Aesar No. 12930, with PDDA) annealed under Ar at 600°C for 12 h, and (d) Ref.-MoO_3 -10×PDDA (Alfa Aesar No. 12930, with 10 times more vol.% PDDA than in (c)), annealed under Ar at 600°C for 3 h. The obtained results indicate the sub-stoichiometry concentration seems to be more dependent on annealing time compared to PDDA concentration.

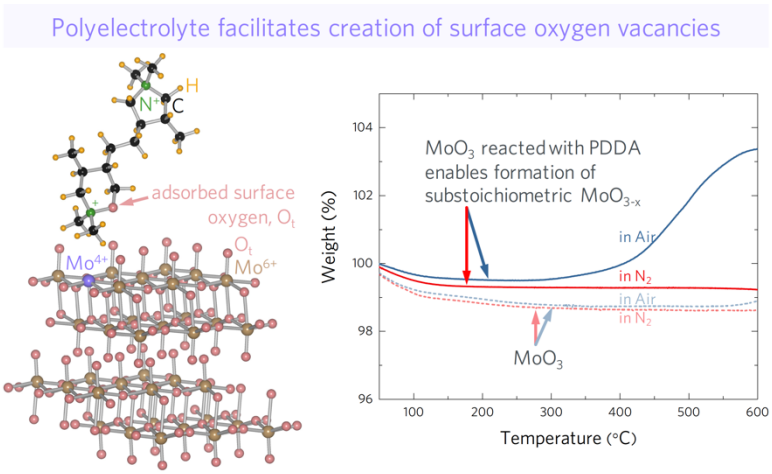

Table of Contents/Abstract Graphic.

Supporting information for

Polyelectrolyte-assisted oxygen vacancies: A new route to defect engineering in molybdenum oxide

Sajad Yazdani,[a,†] Raana Kashfi-Sadabad,[b,†] Tran Doan Huan,[a,c] Mayra Daniela Morales-Acosta [b] and Michael Thompson Pettes[a,b,]*

[a] Department of Mechanical Engineering, University of Connecticut, Storrs, Connecticut 06269, USA.

[b] Institute of Materials Science, University of Connecticut, Storrs, Connecticut 06269, USA.

[c] Department of Materials Science and Engineering, University of Connecticut, Storrs, Connecticut 06269, USA.

[†] These authors contributed equally to this work.

[*] Author to whom correspondence should be addressed, email: michael.pettes@uconn.edu

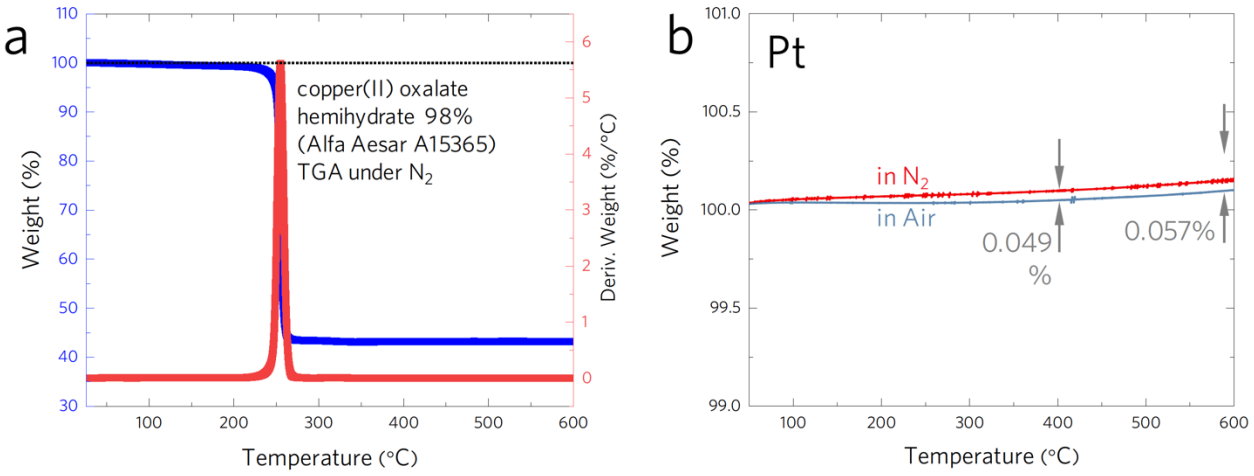

Figure S1. (a) Thermogravimetric analysis (TGA) of copper(II) oxalate hemihydrate 98%, Alfa Aesar No. A15365 under N_2. (b) TGA analysis of Pt under air and N_2. The TGA analysis of Copper(II) oxalate hemihydrate with no oxidation confirms there is no leakage in the TGA instrument. The weight difference between Pt analysis in air and N_2 was used as the error in the MoO_{3-x} weight loss measurements by TGA, where we obtain a confidence value in x of ±0.005.

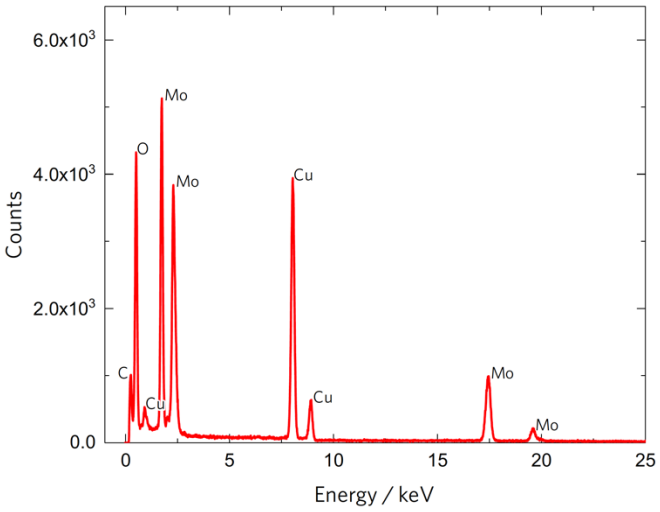

Figure S2. Energy dispersive X-ray spectroscopy (EDS) spectrum of O-MoO_3. The C and Cu peaks arise from beam interactions with the grid and sample holder. No peak from Si was detected, indicating the complete removal of the SBA-15 silica hard template.

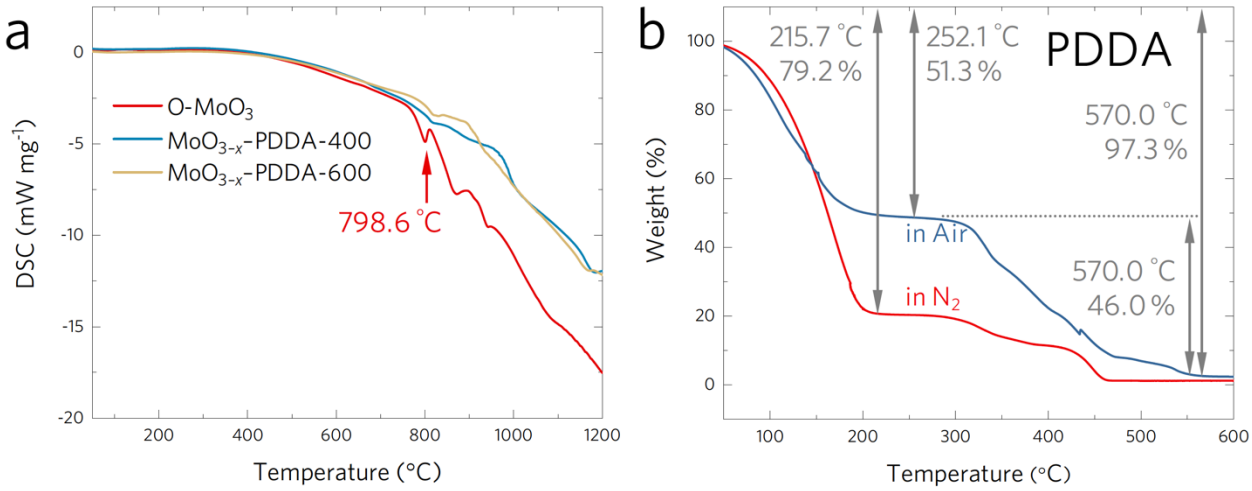

Figure S3. (a) Differential scanning calorimetry (DSC) analysis under argon showing the disappearance of the endothermic phase transition corresponding to melting point of MoO_3 towards higher temperatures in reduced samples MoO_{3-x}–PDDA-400 and MoO_{3-x}–PDDA-600 as compared to the fully oxidized O-MoO_3. This disappearance is due to higher melting points of MoO_{3-x} and MoO_2 compared to MoO_3 (measured at 798.6°C for O-MoO_3). (b) Thermal gravimetric analysis (TGA) of the PDDA polyelectrolyte indicating its decompositions under air and nitrogen atmospheres.

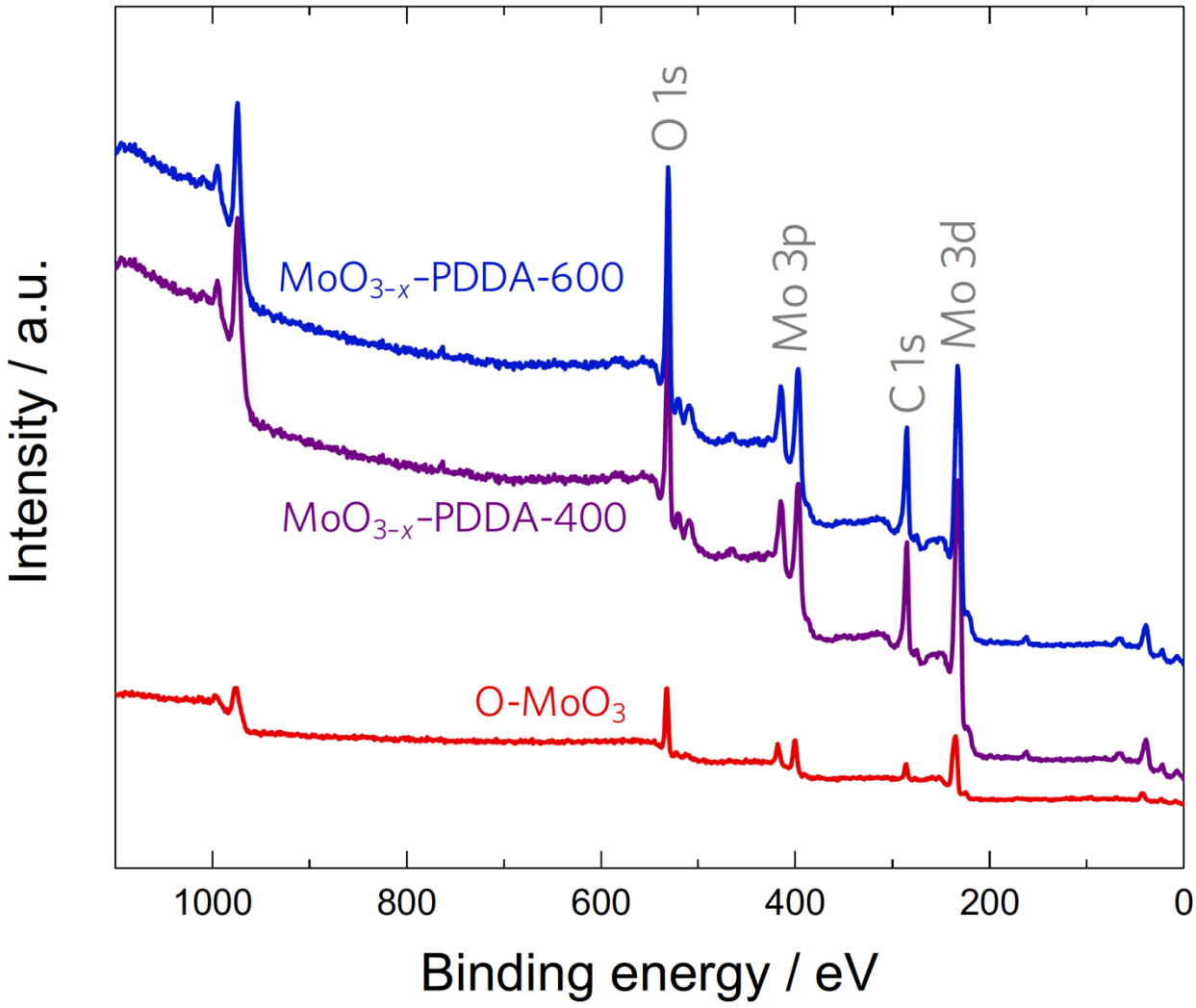

Figure S4. Survey X-ray photoelectron spectroscopy (XPS) spectra of the fully oxidized O-MoO_3, reduced MoO_{3-x}–PDDA-400, and reduced MoO_{3-x}–PDDA-600 samples.

Table S1. Fitting parameters for XPS Mo^{6+}, Mo^{5+}, and Mo^{4+} $3d_{3/2}$ and $3d_{5/2}$ spectral data and peak area ratios.

Sample	Mo^{6+} $3d_{3/2}$		Mo^{6+} $3d_{5/2}$		Mo^{5+} $3d_{3/2}$		Mo^{5+} $3d_{5/2}$		Mo^{4+} $3d_{3/2}$		Mo^{4+} $3d_{5/2}$	
	binding energy (eV)	area (%)	binding energy (eV)	area (%)	binding energy (eV)	area (%)	binding energy (eV)	area (%)	binding energy (eV)	area (%)	binding energy (eV)	area (%)
O-MoO_3	236.34	40.0	233.20	60.0	--	--	--	--	--	--	--	--
MoO_{3-x}–PDDA-400	236.89	7.62	233.20	11.4	234.84	24.8	231.50	37.2	232.99	7.58	229.13	11.4
MoO_{3-x}–PDDA-600	236.77	5.47	233.35	8.2	234.66	14.4	231.21	21.6	232.41	20.1	229.12	30.2
MoO_{3-x}, Inzani *et al.*[S1]	--	--	233.42 233.25	60.1 86.2	--	--	232.22 232.01	39.4 13.8	--	--	229.82	0.5
MoO_{3-x}, Scanlon *et al.*[S2]	235.63	--	232.48	--	--	--	--	--	231.49 (MoO_2)	--	228.29 (MoO_2)	--

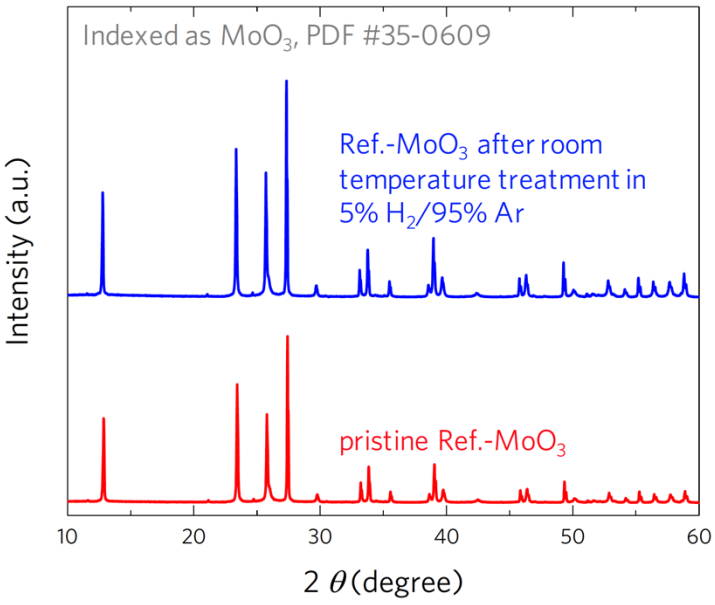

Figure S5. XRD patterns of bulk MoO_3 (Alfa Aesar No. 12930, denoted as Ref.-MoO_3). XRD patterns of the Ref.-MoO_3 pristine sample compared with those of Ref.-MoO_3 kept under 5%H_2/95%Ar gas at room temperature for 12 h. No reduction of MoO_3 is observed with room temperature H_2 treatment.

Supporting references

(1) Inzani, K.; Nematollahi, M.; Vullum-Bruer, F.; Grande, T.; Reenaas, T. W.; Selbach, S. M. Electronic properties of reduced molybdenum oxides, *Phys. Chem. Chem. Phys.* **2017**, *19*, 9232–9245. http://dx.doi.org/10.1039/C7CP00644F

(2) Scanlon, D. O.; Watson, G. W.; Payne, D. J.; Atkinson, G. R.; Egdell, R. G.; Law, D. S. L. Theoretical and experimental study of the electronic structures of MoO_3 and MoO_2, *J. Phys. Chem. C* **2010**, *114*, 4636–4645. http://dx.doi.org/10.1021/jp9093172